POAC'15
Trondheim, Norway

Proceedings of the 23rd International Conference on
Port and Ocean Engineering under Arctic Conditions
June 14-18, 2015
Trondheim, Norway

SHORT-TIME ICE DRIFT AND DEFORMATION MEASUREMENTS USING MULTI-MISSION SYNTHETIC APERTURE RADAR

Thomas Kræmer, Camilla Brekke
Department of Physics and Technology
UiT - The Arctic University of Norway

1. ABSTRACT

Norway is in a good position regarding frequent access to synthetic aperture radar data. A Norwegian–Canadian agreement provides large quotas of RADARSAT-2 images used operationally by e.g. the Norwegian Ice Service. More recently, Norway's participation in the Copernicus program also allows rapid access to SENTINEL-1A data. By combining these data sources we can get satellite time series with very low time separation which allows us to study ice drift, deformation and ice growth processes with a time resolution of minutes and hours rather than days. This allows us to measure the drift of fast moving ice which is usually not observable due to insufficient time sampling. We study ice drift derived using varying time separations ranging from minutes to one day and show the effect on estimated ice speeds. The derived drift is used to construct deformation maps showing areas of converging and diverging ice. We show that very high time resolution is sometimes necessary for measuring fast moving ice. We focus on a particular example that illustrates how low time sampling implies missing significant changes in deformation within one day.

2. INTRODUCTION

Sea ice drift is an important parameter in climate studies for quantifying the motion and outflow of sea ice from the Arctic basin (Spreen et al., 2011). When combined with ice type and thickness measurements it allows us to calculate the volume flux of ice through the main exits from the Arctic. The largest outflow, which also exhibits the highest drift speeds, is Fram Strait between Greenland and Svalbard.

Ice drift information is also valuable as input to forecast models for ice management systems. The objective of ice management is to minimize the impact of drifting ice on fixed or floating installations. An efficient ice management system needs good predictive models which can be incorporated into feed-forward loops when engaging ship thrusters to withstand forcing from drifting ice. To have high predictive power, the input to forecast models must be of sufficient accuracy as well as spatial and temporal resolution. The time resolution becomes increasingly important because conditions in the Arctic can change dramatically over a period of hours. With a shift in the general ice regime towards thinner ice, which is more sensitive to wind forcing, tracking the ice will become more difficult if the time sampling is not increased (Spreen et al., 2011).

Sea ice drift fields have been routinely estimated for two decades by cross-correlating image pairs using data from mainly passive microwave and, more recently synthetic aperture radar (SAR) systems which are active sensors (see Berg and Eriksson, 2013 and references therein). SAR, being an active instrument capable of sensing through cloud cover, is a good compromise between requirements of wide coverage, high resolution and all-weather, day and night imaging. In recent years satellite remote sensing programs have shifted their focus from single satellites to satellite constellations. Cosmo SkyMed is already up and running with four satellites, the Sentinel constellations launched their first satellite in 2014 and the first satellite in the RADARSAT constellation mission is planned for 2018. This will provide unprecedented possibilities for observing rapid changes in the sea ice cover with high spatial and temporal resolution. As an example of what is possible today in terms of time resolution using multi-mission spaceborne SAR, consider fig. 1 which shows potential scenes in a 24-hour window over an area in Fram Strait. By combining (in this case) images from 7 satellites it is possible to obtain 18 images

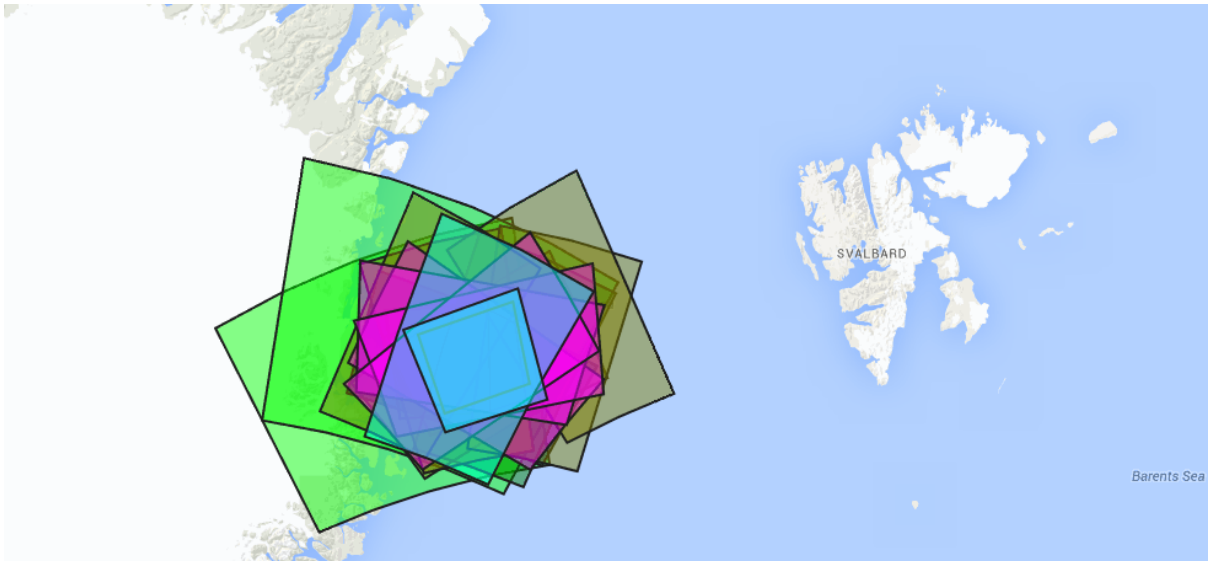

Figure 1: Example of the coverage of SAR images over a period of 24 hours for an area in Fram Strait. The set includes possible footprints from TerraSAR-X, Cosmo SkyMed-1, 2 and 3, RADARSAT-2 and RISAT-1 and SENTINEL-1A.

within a day. However, the cost of satellite imagery is still high, which makes national agreements like the Norwegian–Canadian RADARSAT-2 agreement and involvement in programs like Copernicus very important.

We collected a dataset consisting of 4 SENTINEL-1A scenes and one RADARSAT-2 scene during a 24 hour period on March 13, 2015 (see table 1). The subset of the scenes that provided the best spatial and temporal overlap was then selected to form the basis of our analysis. The paper is organized as follows. We first give a brief introduction to the motion estimation algorithm (section 3) and how we derive deformation maps from the resulting vectors (section 4). In section 5 we show estimated sea ice drift using images with a time separation ranging from 36 minutes to one day. We show that there can be significant changes within a day that are only visible using high time sampling. Finally, we briefly discuss limitations of the use of spaceborne satellites in the context of Arctic operations and some interesting new ways of measuring sea ice drift. Section 6 provides some concluding remarks.

3. ICE DRIFT ESTIMATION

We measure ice drift from times series of SAR satellite images using cross-correlation between small image blocks (Komarov and Barber, 2014). *Phase correlation* (PC) relies on the Fourier shift theorem and performs cross-correlation in the frequency domain. The theorem states that if an image $f_1(\boldsymbol{x})$ is shifted by $\boldsymbol{x_0} = (x_0, y_0)$ such that $f_2(\boldsymbol{x}) = f_1(\boldsymbol{x} - \boldsymbol{x_0})$, then the Fourier transforms $\mathcal{F}_1(\boldsymbol{\omega})$ and $\mathcal{F}_2(\boldsymbol{\omega})$ of f_1 and f_2 respectively are related by

$$\mathcal{F}_2(\boldsymbol{\omega}) = \mathcal{F}_1(\boldsymbol{\omega}) e^{-j\boldsymbol{\omega}\cdot\boldsymbol{x_0}} \tag{1}$$

where $\boldsymbol{\omega} = (\omega_x, \omega_y)$ denote angular frequencies along each image axis and $\cdot$ denotes the scalar inner product between two vectors. The *normalized cross-power spectrum* which implements a combined whitening and cross-correlation reduces to

$$C(\boldsymbol{\omega}) = \frac{\mathcal{F}_1^*(\boldsymbol{\omega})\mathcal{F}_2(\boldsymbol{\omega})}{|\mathcal{F}_1^*(\boldsymbol{\omega})\mathcal{F}_2(\boldsymbol{\omega})|} = e^{-j\boldsymbol{\omega}\cdot\boldsymbol{x_0}} \tag{2}$$

where z^* indicates the complex conjugate of the complex number z. The inverse Fourier transform of eq. (2) is a Kronecker delta function centered at (x_0, y_0), which we call the phase correlation response

$$PC(\boldsymbol{x}) = \mathcal{F}^{-1}\{C(\boldsymbol{\omega})\} = \delta(\boldsymbol{x} - \boldsymbol{x_0}) \tag{3}$$

Table 1: List of scenes used in the experiments.

Tag	Sensor	Mode	Center inc. angle [deg]	Sensing time (UTC)	Time lag from S1
S1	SENTINEL-1A	Extra Wide Swath	34	2015-03-13 05:41:00	
R1	RADARSAT-2	ScanSAR Wide	37	2015-03-13 06:17:41	36 min
S2	SENTINEL-1A	Extra Wide Swath	34	2015-03-13 07:19:13	1 hr 38 min
S3	SENTINEL-1A	Extra Wide Swath	34	2015-03-13 13:50:57	8 hr 9 min
S4	SENTINEL-1A	Extra Wide Swath	34	2015-03-14 06:21:45	1 day 40 min

In practice, deformations of the ice and speckle noise in the images does not allow a sharp registration (delta response) of two image blocks and we observe a noisy and broadened peak. Therefore we use the maximum value of the phase correlation response image instead:

$$(\hat{x}_0, \hat{y}_0) = \arg \max_{\text{(x,y)}} PC(\boldsymbol{x}) \tag{4}$$

We estimated all vectors independently and only matches which had a narrow and strong peak in PC were accepted.

Advances in drift estimation algorithms have largely focused on ways to account for the low time separation e.g. by incorporating multi-resolution analysis to handle large displacements and rotation estimation as well as tracking of flow outlines to handle the marginal ice zone (Berg and Eriksson, 2013; Komarov and Barber, 2014). Other important work has been concerned with assessing the reliability of the derived vectors (Hollands et al., 2014). In our study, the time separation is small, so even with high speeds, the total displacement is limited. However, rotation of the ice can be large enough to prevent matching, even when the images are only hours apart. We therefore include estimation and correction for rotations in the algorithm as in (Komarov and Barber, 2014). Still, we observe that even for images which are close in time the deformation of the ice can be large enough to prevent matching.

Rapid changes in surface conditions of the ice as well as varying imaging geometries means that even images with a small time separation can have appear significantly different. Figure 2 serves as an example, showing subsets of images S1 and S3 (see table 1) North of Svalbard which are separated by 8 hours. In figure 2a, it is relatively easy to identify floe outlines, whereas in figure 2b the ice surface appears much smoother and the main identifiable features are the leads.

4. DEFORMATION

Interpretation of the raw vector fields is often not the primary interest. It is important to quickly identify deformation areas in the form of opening and closing of leads, e.g. to identify better ship routes through the ice. We used the method proposed by Bouillon and Rampal, 2015 to compute deformation related parameters like the divergence of the flow field from the estimated drift.

Given a set of estimation positions $\{(x, y\}$ and estimated velocities $u(x, y)$ in the x-direction and $v(x, y)$ in the y-direction we construct a triangular tesselation over the points and calculate the shear ϵ_{shear}, divergence ϵ_{div} and total deformation ϵ_{td} for each triangle as

$$\epsilon_{\text{shear}} = \sqrt{(u_x - v_y)^2 + (u_y + v_x)^2} \tag{5a}$$

$$\epsilon_{\text{div}} = u_x + v_y \tag{5b}$$

$$\epsilon_{\text{td}} = \sqrt{\epsilon_{\text{shear}}^2 + \epsilon_{\text{div}}^2} \tag{5c}$$

However, we limit the discussion to the divergence ϵ_{div} in this paper. Each triangle is considered as a closed curve oriented counter-clockwise and

$$\begin{aligned} u_x &= \frac{1}{A} \oint u \, \mathrm{d}y \qquad & u_y &= -\frac{1}{A} \oint u \, \mathrm{d}x \\ v_x &= \frac{1}{A} \oint v \, \mathrm{d}y \qquad & v_y &= -\frac{1}{A} \oint v \, \mathrm{d}x \end{aligned} \tag{6}$$

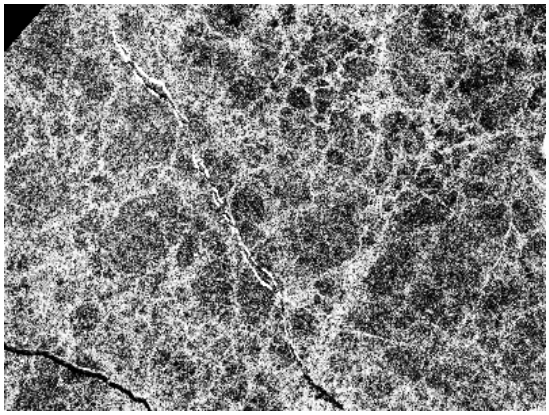

(a) Subset of S1.

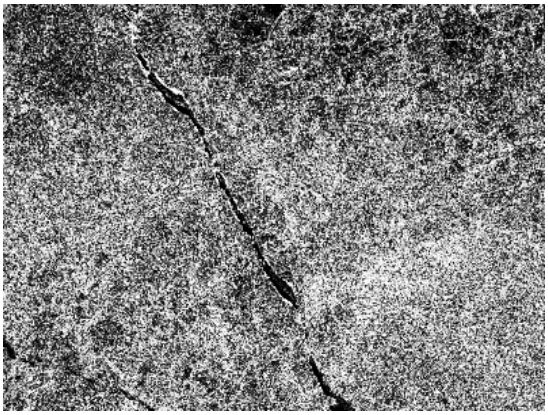

(b) Subset of S3.

Figure 2: Two images approximately 8 hours apart can look significantly different due to changes in surface conditions and imaging geometry. Only a few features like the lead in the middle are easily recognizable.

denote the spatial derivatives for the different vector components of a given triangle in the tessellation.

Estimation of the deformation parameters is very sensitive to noise. Therefore, we smoothed the estimated flow field using a median filter with a radius of 5 km before calculating eq. (5).

5. RESULTS AND DISCUSSION

In this section we look at the ice drift derived from pairs of SAR images with varying time separation, acquired North East of Svalbard on March 13, 2015. Figure 3 shows subsets of each image in table 1 over an area where we found significant deformation. Image S1 (Figure 3a) is used as a reference image and we estimate the drift using the pairs S1–R1, S1–S2, S1–S3, S1–S4, i.e., between the reference image and each of the bottom four images.

On a first glance, the first three images appear very similar, which is not unexpected since the scenes were acquired less than two hours apart. However, closer inspection reveals that there is a slight opening of the long lead which is clearly visible close to the center of each image. There are a set of broader, but shorter leads on the right hand side of the images which also show a slight opening. These changes are difficult to spot without overlaying and animating the images, however.

Changes in the bottom two images (S3 and S4) are more easily identified. Figure 3d shows further opening of the large leads in the top right corner, but the leads in the bottom part are closing. We also see a change in the backscatter to the right of the long lead, where two floes that were difficult to identify in the previous images are now clearly visible. The last image (figure 3e) shows the largest change as almost all the leads have closed.

Figure 4 show flow fields estimated from each image pair with derived divergence maps superimposed. Red areas indicate positive divergence, i.e., opening and blue areas indicate negative divergence, i.e., closing. The measured flow is consistent with what we observe visually when looking at animations of the motion. In the top two plots we can see three regions of different flow (both speed and direction), separated by clearly visible open leads. In the left part, the ice is moving slowly towards the East. The top right part also shows the ice drifting eastwards, but at a slightly faster pace. Finally, the ice in the bottom right corner is drifting much faster towards the South-East. These two images show motion estimated using a time separation of 36 minutes and 1 hour and 38 minutes, respectively. Over this time period the motion is relatively stable, and both pairs show a slight opening of all the lead.

The bottom two images show the motion and divergence calculated between S1–S3 and S1–S4. Figure 4c shows drift estimated from images 8 hours apart and we see a change in the flow direction in the bottom right corner. Where the ice was moving towards the South-East in the top two cases, the direction is now southward and slightly westward. This means that the ice is closing in the bottom part

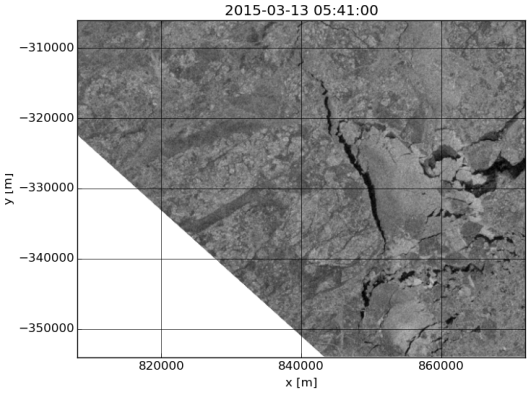

(a) S1 (Reference image).

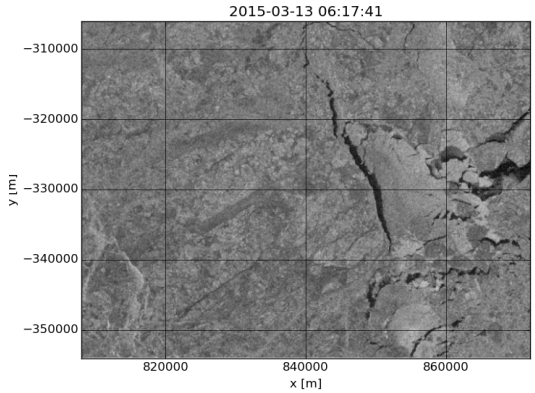

(b) R1

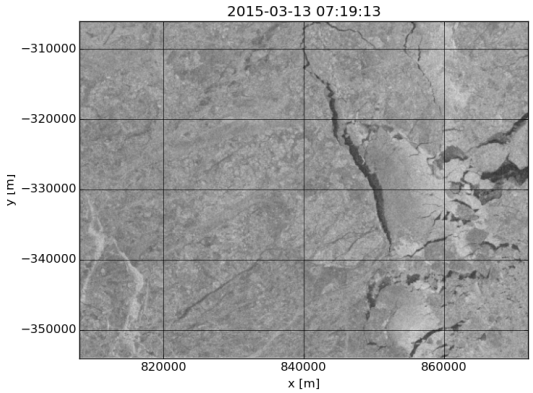

(c) S2

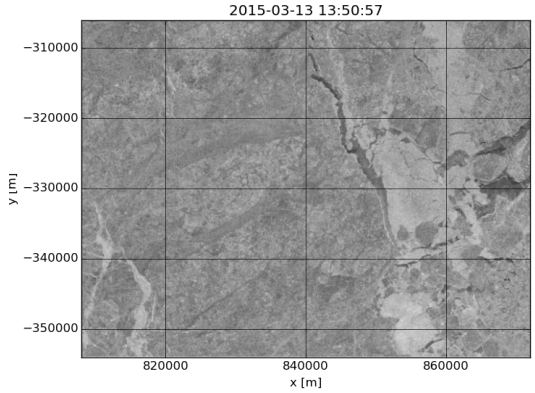

(d) S3

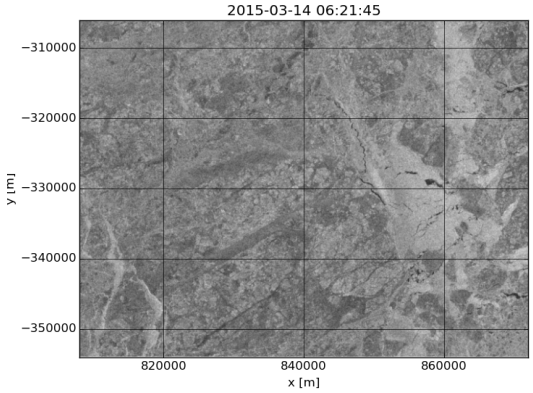

(e) S4

Figure 3: Subsets of the images in table 1 ordered by acquisition time. The leads in the images are opening in the first four images and almost completely closed in the last image. The images are in a polar stereographic projection with North up and East to the right.

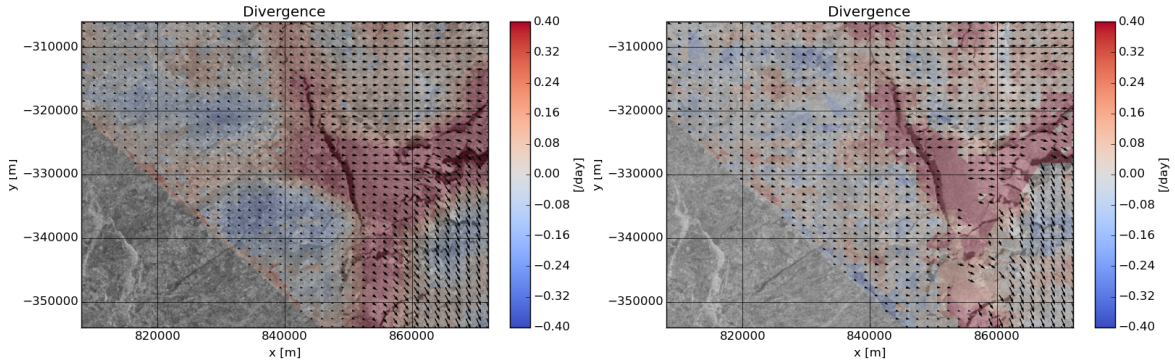

(a) S1–R1

(b) S1–S2

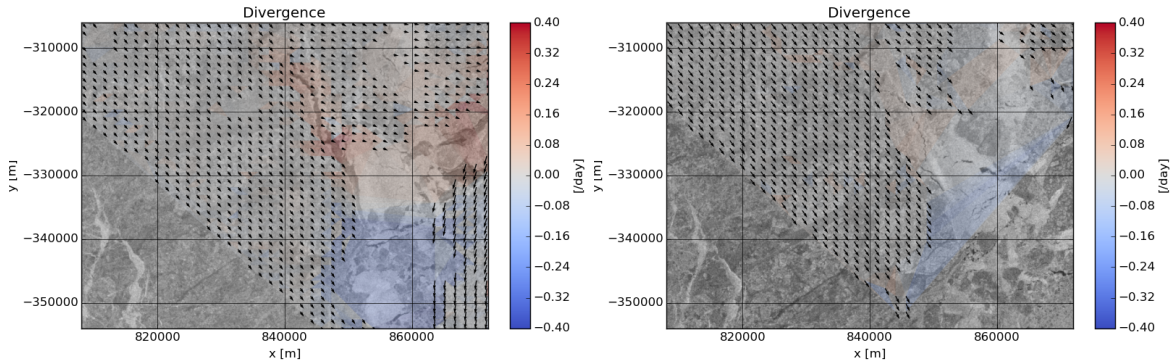

(c) S1–S3

(d) S1–S4

Figure 4: Divergence derived from flow fields obtained by tracking from the first image (S1) to each of the others with increasing time spacing (four lower images in fig. 3). Red (positive divergence) indicates opening and blue indicates closing. Very small values have been masked to better show the underlying image. The lack of vectors in the bottom left corner is because the region is from the edge of the reference image (see figure 3a).

of the area while the large lead is still opening slightly, which is shown in the divergence maps also. At this point, however, the deformation has started to affect the pattern constancy and the algorithm has discarded unreliable matches in the region where the ice is converging (note the lack of vectors in some parts of the blue colored region). Qualitatively, the divergence maps are reasonable, but the lack of motion vectors in the deformation zone adds uncertainty to the divergence measurements.

In the final (bottom right) plot, the displacement and deformation is very strong. The drift direction in lower right area has changed slightly again and is moving rapidly towards the South-West forming a strong front which causes all leads to close. Changes in the patterns and (in some areas) lack of pattern over the ice prevented the algorithm from obtaining many matches in the this area. This of course adds much uncertainty to the deformation maps. The blue region correctly identifies convergence of the ice, but it is based on only a few vectors and the value cannot be trusted. Also, the large lead that was clearly visible, but which is now closed has not been identified as converging. This is likely also a result of missing vectors along the lead, due to missing unique patterns to match. The lack of distinctive patterns on the right hand side of the lead means that we are not able to estimated displacements on both side of the lead.

Ice drift has traditionally been monitored with a time separation of 1–3 days between images. It is interesting to note that with this time spacing the opening of the leads during the 8 hours covered by the first four images would be completely missed. It is clear that to follow rapid changes as in the presented example one must increase the time spacing to preserve the pattern constancy required by the matching algorithm. Since leads in the ice is an interface of heat transfer between the ocean and atmosphere, missing such events is likely to introduce biases in coupled ocean–ice–atmosphere models.

Frequent satellite acquisitions are not only an advantage for operational purposes, but the drift estimation algorithms will typically perform better if the time separation between scenes is less than one day. However, this is true only up to a point as correlation tracking algorithms have difficulties measuring sub-pixel displacements. It has been noted by Hollands and Dierking, 2011 that correlation algorithms perform poorly over either slow moving or fast ice. For scenes with a small time separation this can become an issue even with fast moving ice. Small time separation means we need to start paying close attention to geocoding accuracy as well. The combined effects of speckle, deformation of the ice, tidal variations and uncertainty related to the sensor-target geometry means we need ice displacement of several pixels before we can trust that the measured displacement is a physical displacement and not induced by processing.

Using the full images in table 1 (as opposed to the subsets shown in fig. 4) we looked at how drift speeds varied with different time spacings. Figure 5 shows normalized histograms of the estimated drift speeds for the four pairs. We see that the low time separation of 37 minutes is able to expose high drift speeds (up to 60 cm/s) than what we observe with longer time separation. For longer time separations, both the mode and the range of the speed distribution move toward lower speeds (3–10 cm/s). The high speeds were mainly observed in the marginal ice zone and as bands of ice floating in open water while the pack ice had a relatively consistent drift speed less than 0.1 m/s.

The advantage of the small time separation easy to see–we can measure high drift speeds which are normally only observable with buoys. Although we are able to obtain high temporal resolution the images are not uniformly spaced in time, i.e. we get a pair of scenes only minutes apart, then we may have to wait for 12 hours to get the next scene. For ice drift it would be useful to have more uniform spacing between acquisitions.

5.1 Alternative sources of drift using SAR

Although the ice drift fields themselves are useful for model calibration, they are not the only relevant measurement. Wind is the main force driving the ice drift and information on wind conditions is equally important for modelling ice drift and deformation. With the launch of new and improved SAR satellites, new possibilities for measuring both ice drift and wind are opening up. Chapron et al., 2005 showed that the radial (line-of-sight) surface velocity of scatterers on the ocean surface could be extracted by

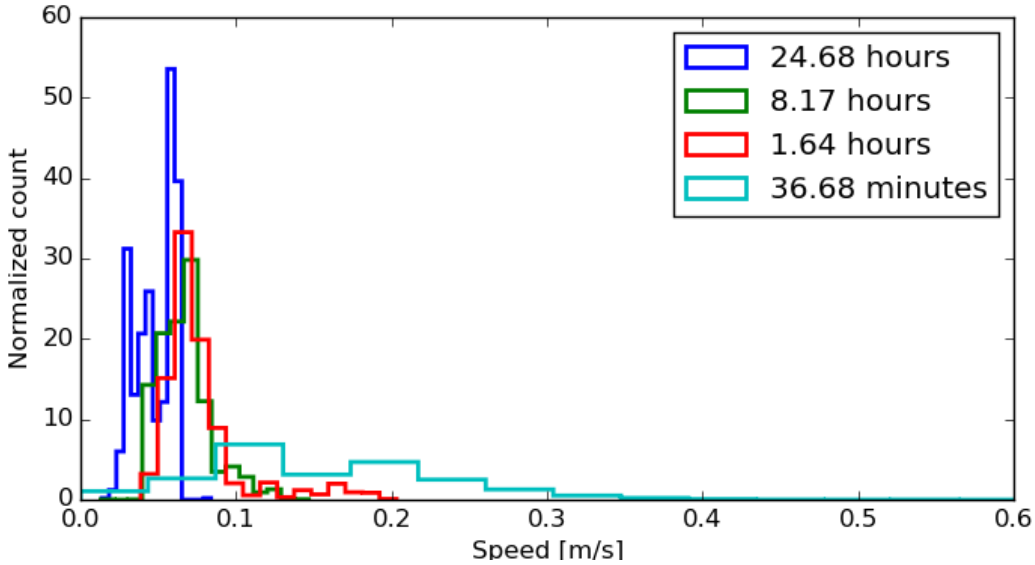

Figure 5: Normalized histogram of ice drift speeds for different time spacings within the same day. It is possible to observe high drift speeds of 0.6 m/s directly from satellite when using images that are close in time. The effect of lowering the time sampling is evident on the derived speeds.

measuring the deviation of the SAR signal Doppler shift from the expected Doppler shift due to the relative sensor-target motion.

The technique was initially developed with applications to ocean wind and current estimation using the ENVISAT ASAR instrument. For C-band, empirical relations exist relating the Doppler centroid anomaly to wind (Mouche et al., 2012). It will be interesting to see how this information can be incorporated into models of the Arctic to support ice drift modelling. The interpretation of these line-of-sight velocities are still not well-understood and more work will be required before this can be used directly. However, the ASAR was not designed with this in mind and the precision of the method was therefore affected. New sensors like SENTINEL-1A implement fine control over the orbit and attitude of the antenna through *total zero-Doppler steering* (Fiedler et al., 2005). This allows us to measure the radial surface velocity from the SAR signal with unprecedented precision. As an example, fig. 6 shows the line-of-sight motion (right) estimated from a SENTINEL-1A Extra Wide (EW) scene over Svalbard on January 23, 2015 along side the intensity image (left). Negative values (blue/green) indicates drift away from the antenna and positive values (yellow/red) indicate drift towards the antenna. Note the strong diagonal front clearly visible in the image.

It is difficult to measure the ice drift speed directly using this method, because it requires fast moving ice and ice drift oriented along the antenna pointing direction. However, it is possible under favorable conditions (see Kræmer et al., 2015). An advantage of measuring the movement directly from the SAR signal is that no pattern matching takes place. Rather, the drift information is derived from a single image and does not rely on an assumption of pattern constancy. In any case, surface velocity over ocean should still provide valuable information that can be used together with other information to predict wind direction and the subsequent push on the ice.

It is also possible to obtain the radial surface velocity using interferometric techniques. Like the Doppler, this will also give line of sight drift, but at much higher spatial resolution. This was shown using TanDEM-X, but the requirement of two satellites in close formation makes this method infeasible for operational use (Scheiber et al., 2011; Romeiser et al., 2013).

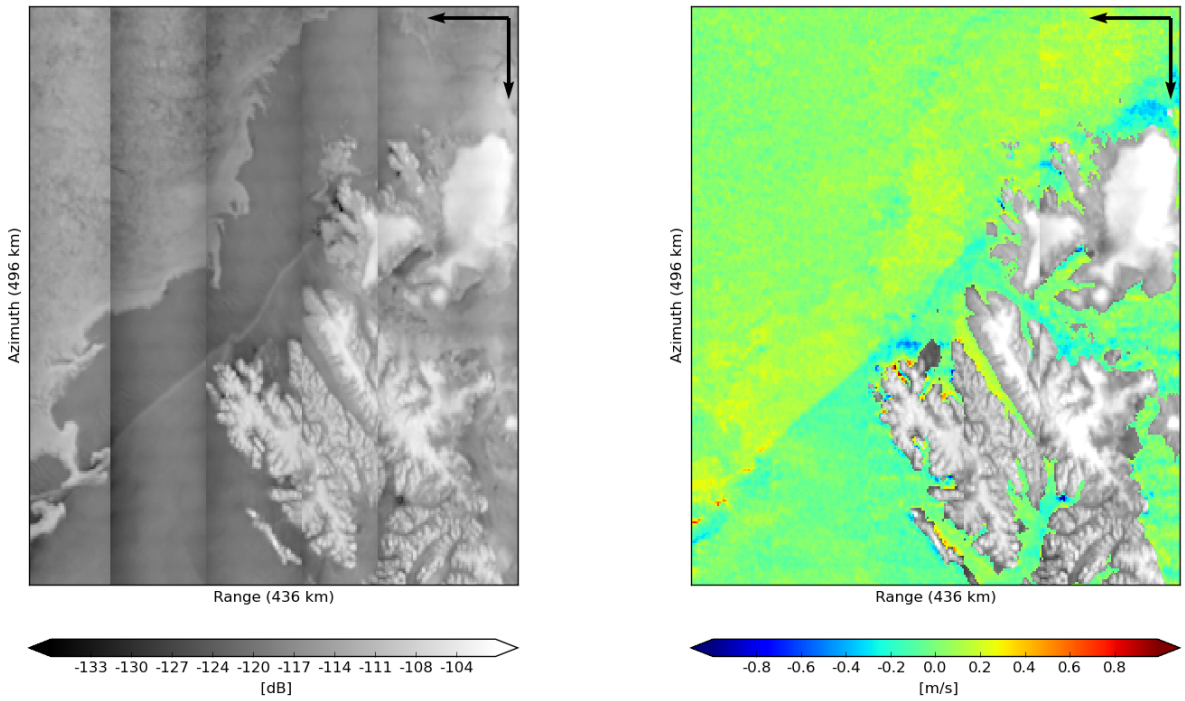

(a) Backscatter intensity image.

(b) Ground range radial surface velocity.

Figure 6: Estimated radial surface velocity from a SENTINEL-1A EW scene showing instantaneous surface motion along the antenna pointing direction. The scene is a right-looking acquired in a descending pass (indicated by black arrow).

6. CONCLUSION

We have demonstrated the combination of multiple sensors for measuring fast moving ice drift, traditionally only observable using buoys. Because it takes roughly 100 minutes for most SAR satellites to partly cover the same geographical area at high latitudes it is useful to take advantage of multiple missions to capture higher drift speeds over extended areas. We demonstrated that the typical temporal resolution for ice drift measurements (a day or more) can mask rapid opening and closing of the ice. We discussed briefly how modern SAR satellite constellations will play a central role in improving the temporal and spatial resolution and coverage.

ACKNOWLEDGEMENTS

This work is supported by the Arctic Earth Observation and Surveillance Technologies (Arctic EO) project 195143 under contract of the Norwegian Research Council. SENTINEL-1A data are reprovided through the Copernicus program/European Space Agency (2015). RADARSAT-2 Data and Products ®MacDONALD, DETTWILER AND ASSOCIATES LTD. (2015) – All Rights Reserved. RADARSAT is an official mark of the Canadian Space Agency.

REFERENCES

Berg, Anders and Leif E. B. Eriksson (2013). "Investigation of a Hybrid Algorithm for Sea Ice Drift Measurements Using Synthetic Aperture Radar Images". In: *IEEE Transactions on Geoscience and Remote Sensing*, pp. 1–11.

Bouillon, S. and P. Rampal (2015). "On producing sea ice deformation data sets from SAR-derived sea ice motion". In: *The Cryosphere* 9.2, pp. 663–673.

Chapron, Bertrand, Fabrice Collard, and Fabrice Ardhuin (2005). "Direct measurements of ocean surface velocity from space: Interpretation and validation". In: *Journal of Geophysical Research* 110.C7, pp. 1–17.

Fiedler, H. et al. (2005). “Total Zero Doppler Steering—A New Method for Minimizing the Doppler Centroid”. In: *IEEE Geoscience and Remote Sensing Letters* 2.2, pp. 141–145.

Hollands, Thomas and Wolfgang Dierking (2011). “Performance of a multiscale correlation algorithm for the estimation of sea-ice drift from SAR images: initial results”. In: *Annals of Glaciology* 52.57, pp. 311–317.

Hollands, Thomas, Stefanie Linow, and Wolfgang Dierking (2014). “Reliability Measures for Sea Ice Motion Retrieval From Synthetic Aperture Radar Images”. In: *IEEE Journal of Selected Topics in Applied Earth Observations and Remote Sensing* 8.1, pp. 67–75.

Komarov, Alexander S. and David G. Barber (2014). “Sea ice motion tracking from sequential dual-polarization RADARSAT-2 images”. In: *IEEE Transactions on Geoscience and Remote Sensing* 52.1, pp. 121–136.

Kræmer, Thomas, Harald Johnsen, and Camilla Brekke (2015). “Emulating Sentinel-1 Doppler Radial Ice Drift Measurements using Envisat ASAR Data (accepted)”. In: *IEEE Transactions on Geoscience and Remote Sensin*, pp. 1–12.

Mouche, Alexis A. et al. (2012). “On the Use of Doppler Shift for Sea Surface Wind Retrieval From SAR”. In: *IEEE Transactions on Geoscience and Remote Sensing* 50.7, pp. 2901–2909.

Romeiser, Roland et al. (2013). “Quality Assessment of Surface Current Fields From TerraSAR-X and TanDEM-X Along-Track Interferometry and Doppler Centroid Analysis”. In: *IEEE Transactions on Geoscience and Remote Sensing* PP.99, pp. 1–14.

Scheiber, R et al. (2011). “Interferometric sea ice mapping with TanDEM-X: First experiments”. In: *International Geoscience and Remote Sensing Symposium (IGARSS)*, pp. 3594–3597.

Spreen, Gunnar, Ron Kwok, and Dimitris Menemenlis (2011). “Trends in Arctic sea ice drift and role of wind forcing: 1992-2009”. In: *Geophysical Research Letters* 38.19, n/a–n/a.